

# Modeling and Measurement of Rainfall by Ground-Based Multispectral Microwave Radiometry

Frank Silvio Marzano<sup>1</sup>, *Senior member IEEE*, Domenico Cimini<sup>1</sup>, *member IEEE*,  
Piero Ciotti<sup>1</sup>, *member IEEE*, and Randolph Ware<sup>2</sup>

<sup>1</sup> Center of Excellence CETEMPS, University of L'Aquila  
Monteluco di Roio, 67040 L'Aquila, Italy  
E-mail: marzano@ing.univaq.it, nico.cimini@aquila.infn.it, ciotti@ing.univaq.it  
fax +39.0862.434403

<sup>2</sup> Radiometrics Corp. and University Corporation for Atmospheric Research  
Boulder, Colorado, USA  
E-mail: ware@radiometrics.com

*Corresponding author:* Frank Silvio Marzano

**Paper n. 00225**

**Accepted**

**Trans. on Geoscience and Remote Sensing  
MicroRad04 Special Issue**

**October 2, 2004**

**Abstract** – The potential of ground-based multispectral microwave radiometers in retrieving rainfall parameters is investigated by coupling physically oriented models and retrieval methods with a large set of experimental data. Measured data come from rain events that occurred in the USA at Boulder, Colorado, and at the Atmospheric Radiation Measurement (ARM) Program's Southern Great Plains (SGP) site in Lamont, Oklahoma. Rain cloud models are specified to characterize both non-raining clouds, stratiform and convective rainfall. Brightness temperature numerical simulations are performed for a set of frequencies from 22 to 60 GHz at zenith angle, representing the channels currently deployed on a commercially available ground-based radiometric system. Results are illustrated in terms of comparisons between measurements and model data in order to show that the observed radiometric signatures can be attributed to rainfall scattering and absorption. A new statistical inversion algorithm, trained by synthetic data and based on principal component analysis is also developed to classify the meteorological background, to identify the rain regime, and to retrieve rain rate from passive radiometric observations. Rain rate estimate comparisons with simultaneous rain gauge data and rain effect mitigation methods and results are also discussed.

**Keywords:** Microwave radiometry, rainfall, ground-based remote sensing, atmospheric retrieval, radiative transfer.

## **OUTLINE**

### **I. Introduction**

### **II. Experimental data**

### **III. Radiometric signature of rainfall**

- A. Rain radiative models
- B. Comparison with radiometric data

### **IV. Radiometric estimation of rainfall**

- A. Inversion techniques
- B. Comparison with rain gauges

### **V. Summary and future developments**

### **References**

### **Acknowledgements**

### **Authors' biographies**

### **Table and figure captions**

### **List of tables and captions**

## **I. INTRODUCTION**

Ground-based microwave radiometry has been mainly investigated for estimating temperature, water vapor and cloud liquid profiles in the absence of precipitation [1]-[2]. The increasing use of multi-frequency radiometers in ground-based meteorological and receiving stations has raised the question of their potential for retrieving rainfall parameters [3]-[8]. This feature is even more appealing if the ground-based microwave radiometer can be equipped by automatic scanning in order to cover a large atmospheric volume in a manner similar to radar systems. Indeed, synergetic use of radiometric rain retrieval methods with weather radar systems is another important application, especially with constrained path-attenuation mitigation techniques [8].

Ground-based microwave radiometry as compared to radar has the advantage of lower procurement and maintenance costs, with the disadvantage that the rain product is not range-resolved. On the other hand, rainfall retrieval by satellite-based microwave radiometry is limited by its relatively coarse spatial resolution as well as beam filling effects and a relatively low sensitivity over land, but has the advantage of global coverage [9]. Finally, rain gauges make a point measurement of rainfall at ground level. Indeed, the extreme variability of precipitation in time and space lends difficulty to its accurate retrieval since all known methods have their strengths and weaknesses for meteorological and hydro-geological applications. In a synergetic approach ground-based microwave radiometry is a potentially useful complementary tool [6]-[8].

The exploitation of ground-based microwave radiometry raises both modeling and experimental issues. From a modeling point of view, the approach to rainfall signature characterization requires a thorough insight into the electromagnetic interaction between the microwave radiation and the scattering medium since the radiometric response depends on the various radiative sources along the observation path [5], [7]. With respect to an empirical inversion technique trained by measured observables and parameters [4], [6], the accuracy of a physically based retrieval approach relies on modeling capability to take into account multiple scattering and atmospheric inhomogeneity due to hydrometeors in different phases [7]-[8], [10]. From an experimental point of view, one of the main problems of ground-based radiometric retrieval of rainfall is contamination generated by liquid water on the receiving antenna. In order to solve this problem, hardware solutions [11], [12] or robust inversion techniques [5], [8] can be foreseen.

An appealing objective of current research is to extract rainfall signatures and parameters in a quantitative way from multispectral ground-based microwave radiometric measurements. Previous work used observations from a three-channel microwave radiometer [5], [8]. As explained in Sect. II, in this work we use observations from 12-channel radiometers that are currently operational in various sites around the world [13]. Rain events that occurred at Boulder, Colorado, and near Lamont, Oklahoma, at the Atmospheric Radiation Measurement (ARM) Program Southern Great Plains (SGP) site have been analyzed on a temporal period including nearly one year of continuous measurements. Observations from a rain gauge at the same location were coordinated with the radiometric measurements.

In order to exploit the information content of the 12-channel radiometric system, we have adopted a retrieval approach based on a physical radiative model able to characterize both stratiform and convective precipitation, including spherical liquid, melt, and ice hydrometeors [5], [8]. The model is further described in Sect. III. By varying and properly tuning the forward model parameters at the measurement sites in a physically based manner, a synthetic cloud radiative database has been derived that is based on the downwelling simulated brightness temperatures ( $T_B$ 's), the associated mean radiative temperature and the total path-attenuation. In addition, a new non-linear statistical inversion procedure has been developed that is based on successive steps where rainfall is (1) detected, (2) classified with respect to its regime, and (3) estimated in terms of columnar water and rain rate. Results are illustrated by means of comparisons between multispectral measurements and model data in order to show that the observed radiometric signatures can be attributed to rainfall scattering and absorption. Finally in Sect. IV, rain rate radiometric estimates are compared with available simultaneous rain gauge data, showing the potential of the technique to retrieve rainfall parameters, followed by a discussion about the limitations of this intercomparison and on possible effects of antenna water-film mitigation techniques.

## II. EXPERIMENTAL DATA

As already mentioned, in order to interpret and test rainfall model simulations and rain rate estimates, a fairly large set of measurements, acquired by MicroWave Radiometer Profilers (MWRP's) manufactured by Radiometrics Corp., has been used.

The MWRP radiometer observes the radiation intensity at 12 frequencies in a region of the microwave spectrum that is dominated by atmospheric emissions from water vapor, cloud liquid water, and molecular oxygen. The 12 observation frequencies (i.e., 22.035, 22.235, 23.835, 26.235, 30.00, 51.250, 52.280, 53.850, 54.940, 56.660, 57.290, 58.800 GHz) were chosen by an eigenvalue analysis to optimize retrieval accuracy. Using neural network inversion algorithms the MWRP provides temperature and humidity soundings up to 10 km height and low resolution cloud liquid soundings [9]. The radiometric profiler includes a vertical infrared sensor and surface temperature, humidity, pressure sensors. A rain detector, based on resistive changes of a printed circuit in presence of rain, is also included to identify the presence of liquid water on the radiometer antenna.

As an example, **Fig. 1** shows the operational real-time output printed on the screen by the proprietary MWRP data acquisition and processing software (VizMet®). Contour plots show time-height cross sections of atmospheric temperature, relative humidity and liquid water retrievals. Time series of temperature, relative humidity, and pressure at the instrument level are shown on the left. Time series of infrared cloud temperature, rain detection, integrated content of vapor and liquid are shown at the bottom. An estimate of the cloud base height is also plotted in the upper contour panel. Thus, the operational output allows the user to monitor in real-time ten fields of meteorological interest simultaneously. Data were collected during 19 July 2003, in Boulder, Colorado, USA, including the occurrence of a rain shower which started at roughly 0400 UTC, as revealed by the rain detector, and lasted for about 20 minutes.

Rainfall has a distinct signature on radiometric measurements which appears in a different way if considering either a window or an absorption channel. **Fig. 2** shows the time series of MWRP radiometric observations at its 12 frequency channels during the same period as in **Fig. 1**. A signature of more than 200 K is shown by the window channels. Rain occurrence causes the large increase of measured  $T_B$ 's in the low frequency channels and saturation/depression in the oxygen absorbed band. This behavior is due to the predominance of either emission or scattering in the  $T_B$  signature from ground with respect to the clear-air value, as we will point out in the next section.

For a preliminary statistical validation, about one year of MWRP radiometric observations at the ARM SGP site, from June 2001 to June 2002, have been analyzed in this work. A tipping-bucket rain gauge, part of the ARM Surface Meteorological Observation System (SMOS) has been also available. The rain gauge was located at about 500 m from the MWRP, providing data with a temporal resolution of half an hour and a precision of 0.254 mm with an uncertainty of  $\pm 0.254$  mm. It should be noted that 500 m may be a significant fraction of the correlation distance of convective rainfall (about few kilometers). Unfortunately, no other rain gauges closer to the radiometer and with a faster response were available.

**Fig. 3** characterizes the set of observations in terms of TB histograms at different frequencies. It is evident from the dual-mode distribution of low-frequency  $T_B$ 's that rain cases represent just a small fraction of the entire data set. According to the rain gauge, for the entire data set the total fraction of time when rain

was observed is 174 hours. Channels with strong absorption, like the ones near the oxygen complex centered at 60 GHz, show a small range of variability, since they are close to saturation. On the other hand, channels with weak absorption, such as in the 20-30 GHz range, show a much larger range of variability, since the signals go from 10-20 K to saturation. A detailed analysis of the rainfall microwave signature will be carried out when comparing measured and simulated data in the next section.

### III. RADIOMETRIC SIGNATURE OF RAINFALL

A general theoretical framework for modeling of brightness temperatures generated by clouds and hydrometeors and measured by a microwave radiometer is given by radiative transfer integro-differential equation (RTE) [8], [14]. In the following sections, we briefly summarize characteristics of forward models employed in this work, together with a comparison with measured  $T_B$ 's.

#### A. RAIN RADIATIVE MODELS

A vertically stratified atmosphere with its lowest level at  $z=0$  (surface) and highest level at  $z=H$  (generally around 30 km) is here considered. For convenience we can define a vertical coordinate in terms of optical thickness  $\tau_\nu$  at frequency  $\nu$  such that  $\tau_\nu=\tau_0=k_{e\nu}H$  at  $z=H$  and  $\tau_\nu=0$  at  $z=0$  with  $k_{e\nu}$  the extinction coefficient at frequency  $\nu$ . It is also convenient to introduce the zenith-angle cosine  $\mu=|\cos(\theta)|$  with  $\theta$  the zenith angle.

It is instructive to derive an analytical form of RTE in case of a uniform scattering slab with known optical thickness  $\tau_0$ , temperature  $T_0$ , albedo  $w_0$  and phase function  $p_0$ . For a plane-parallel geometry, the unpolarized azimuthally-symmetric down-welling brightness temperature  $T_B(0,\mu)$ , observed from ground at a frequency  $\nu$ , can be formally expressed by (e.g., [7], [8]):

$$T_B(0,\mu) = T_{BG}e^{-\tau_0/\mu} + T_0(1-w_0)(1-e^{-\tau_0/\mu}) + \frac{w_0}{2\mu} \int_0^{\tau_0} p_0(\mu,\mu')T_B(\tau_\nu,\mu')e^{-\tau_\nu/\mu} d\tau_\nu \quad (1)$$

where  $T_{BG}$  is the cosmic background temperature (about 2.73 K for microwaves) and  $T_0$  the physical temperature. The second term of (1) represents thermal emission, while the third term is sometimes referred to as a multiple scattering source. The atmosphere is generally assumed to consist of  $L$  adjacent homogeneous layers in which volumetric albedo  $w$ , extinction coefficient  $k_e$  and phase function  $p$  are taken to be constant within layers. Note that the numerical solution of (1) assumes knowledge of boundary conditions which implicitly affect the final solution.

The previous equation indicates that when the layer albedo tends to zero, we get the well-known solution for ground-based observations of clear air and non-scattering clouds. When the layer albedo is larger than zero, depending on frequency and layer rain rate, then the equivalent layer temperature (i.e.,  $T_0(1-t)$  with  $t=\exp(-\tau_0/\mu)$  the atmospheric transmittance) tends to be diminished by the increase of the albedo itself, while the incoherent multiple scattering tends to be increased. The solution of (1) when  $w_0=0$  represents the ‘‘clear-air background’’ of the radiometric measurement. This ‘‘clear-air background’’ can play a role in the interpretation of ground-based measurements when considering window (e.g., 20-30 and 50-53 GHz) or absorption (e.g., 54-60 GHz) channels. For window channels the observed clear-air  $T_B$ 's are fairly low, whereas for absorption channels the  $T_B$ 's are relatively high. Note that  $T_B(0,\mu)$  due to rainfall is fairly well correlated with atmospheric optical thickness which is, in its turn, well correlated to columnar rain water contents [3], [5], [8]. The latter, with some time delay (up to 10 minutes depending on rain regime), is related to surface rain rate, typically measured by rain gauge sensors at ground [15].

In previous works we described a technique to use cloud-resolving model output to physically constrain the vertical correlation of hydrometeor content within cloud layers [8], [5], [15]. Briefly speaking, the gross vertical distribution of four species of hydrometeors including cloud droplets, raindrops, graupel particles, and snow particles, has been modeled. Cloud structures have been vertically resolved, within each cloud class, in seven homogeneous layers with fixed levels and a vertical resolution of about 1-1.5 km. The cloud data set, classified into stratiform rain clouds (nimbostratus,  $Ns$ , including strato-cumuli as well), convective rain clouds (cumulonimbus,  $Cb$ ), stratiform non-raining clouds (stratus,  $St$ ), cumuliform non-raining clouds (cumulus,  $Cu$ ), and clear-air ( $Cl$ ), has been then extended by means of a Monte Carlo

statistical procedure. Meteorological variables, such as temperature, humidity and pressure profiles, have been assumed to be uniformly variable around their mean values within a given percentage. Microwave gaseous absorption has been computed by means of the Liebe model [16]. The land-surface emission has been characterized by a Lambertian emissivity model, depending on randomly-variable surface humidity (giving emissivity values between 0.85 and 0.95).

The hydrometeor shapes have been assumed all spherical and characterized by inverse-exponential particle size distributions (PSD's) (see [8] for further details). In the logarithmic plane the intercept of a PSD has been derived from the assigned equivalent water content within each layer, while the slope has been parameterized to surface rain-rate using a Marshall-Palmer, a Sekhon-Srivastava and a Gunn-Marshall PSD for raindrops, ice graupel and snow, respectively. For stratiform rain clouds, a melting layer has been modeled by choosing a water-coated ice-particle model. Indeed, oblateness of raindrops can cause a depolarization signal, depending on cloud stage and wind circulation [7], but it is here considered a second-order effect. Mie absorption and scattering functions have been numerically computed by imposing hydrometeor diameter ranges and densities [8].

In order to generate a fairly large data set to cover a wide range of climatic conditions, the synthetic clouds have been embedded in various meteorological environments which have been tuned to the specific measurement site by collecting available radiosoundings. All meteorological profiles have been supposed to be standard and varied in a random way, with a uniform statistics, around mean values of surface and vertical gradient parameters depending on the season. Mean surface temperatures from 273 to 303 K have been imposed with steps of 5 K and a uniform variability of 10 K around the mean values with a standard gradient of 7.5 K/km (with a uniform variability of 15%). Mean pressure profile have been supposed to be exponential with a surface value of 980 hPa (SPG site reference value) and a uniform variability of 1% of the mean value together with a scale height of 7 km. Humidity was assumed to be close to saturation with an exponential profile having a mean surface value between 7 and 14 g/m<sup>3</sup>, according to the season, with a uniform variability of 15% of the mean value and a scale height of 1.5 km. When imposing the variability of meteorological profiles, the vertical distribution of rain and ice layers has been modified accordingly by imposing some physical criteria such as the absence of ice below the freezing level (except for an explicit melting layer), the prevention of super-saturation, the absence of water above the glaciation level and the limitation of the vertical extension of the rain cloud by using a reduction factor proportional to the temperature difference between the synthesized mean profile and the initial one.

By using the coupled rainfall and radiative transfer model described above, a large classified data set has been simulated, consisting of several thousands of cloud structures together with related brightness temperatures at given frequencies and observation angles. More precisely, the overall simulated dataset, adopted in this work, consists of 35 classes, each with 1000 structures, derived from: (1) 7 meteorological (macrophysical) classes spanning from 0 to 30°C of mean surface temperature with steps of 5°C (named as *m0*, *m5*, *m10*, *m15*, *m20*, *m25*, *m30*), and (2) within each meteorological class, 5 cloud (microphysical) classes categorized as *Cl*, *St*, *Cu*, *Ns* and *Cb* genera. The number of 1000 cloud structures has been chosen as a compromise between computation efficiency and current radiometric system accuracy. The analysis has included the frequency bands of the operational multi-channel radiometer MWRP. The observation angle has been chosen in accordance to the application, in principle between 0 and 90° elevation. Here we will show results only for zenith observations in order to be able to compare simulations with radiometric and rain gauge measurements, as discussed in the next sections.

## B. COMPARISON WITH RADIOMETRIC DATA

A way to represent the ensemble of multispectral signatures in a compact way is to perform a principal component (PC) analysis (e.g., [20]). If  $\mathbf{T}_B$  is a column vector made by 12 TB's measured at the MWRP frequencies (in GHz) at zenith, that is  $\mathbf{T}_B = [T_B(22.035), T_B(22.235), T_B(23.835), T_B(26.235), T_B(30.00), T_B(51.250), T_B(52.280), T_B(53.850), T_B(54.940), T_B(56.660), T_B(57.290), T_B(58.800)]'$ , then  $\mathbf{T}_B$  can be expanded as follows:

$$\mathbf{T}_B - \langle \mathbf{T}_B \rangle = \sum_{i=1}^{12} P_{Bi} \mathbf{e}_{Bi} \quad (2)$$

where the angular brackets stands for ensemble average,  $P_{Bi}$  is the  $i$ -th principal component ( $i=1-12$ ), and  $\mathbf{e}_{Bi}$  is the corresponding  $i$ -th eigenvector ( $i=1-12$ ) or empirical orthogonal function (EOF's) of the  $T_B$  auto-covariance matrix. As known, if  $\lambda_i$  is the  $i$ -th eigenvalue associated to  $i$ -th EOF, then its normalization to the eigenvalue sum represents the dataset explained variance. Note that the convention is such that PC's are ordered with  $P_{B1}$  explaining the highest relative variance.

As an example, by taking into consideration all the simulated dataset, in order to explain the 99% of the variance only the first 3 principal components are needed, with  $P_{B1}$ ,  $P_{B2}$  and  $P_{B3}$  explaining 96%, 2% and 1% of the total variance corresponding to an associated standard deviation of 213, 28 and 6 K, respectively. The information content carried by the first 3 EOF's is shown in **Fig. 4** by plotting the elements of  $\mathbf{e}_{Bi}$  with respect to the frequency band.

It is worth mentioning that EOF1 is mostly affected by a combination of liquid water and water vapor emission, EOF2 tends to weight temperature sounding channels and EOF3 responds basically to water vapor channel. Considering that EOF elements are proportional to the  $T_B$ -PC correlation coefficients, we note that the first PC is fairly correlated with the window-frequency and water-vapor absorption  $T_B$ 's, the second PC is correlated with water-vapor absorption and 60-GHz more transparent channels, while the third PC is correlated with 60-GHz absorbed channels and cloud-liquid channel at 30 GHz. It should be stressed that, when we consider only a cloud class dataset for a given meteorological surface condition, the contribution of oxygen-band channels to the third PC tends to be negligible.

A valuable objective to verify the simulation outputs is to compare radiometric measurements, introduced in Sect. II, with the synthetic data set, described in the previous section. This comparison can give an indication of the realism and physical consistency of the ground-based radiometric simulations over a wide span of microwave frequencies.

**Fig. 5** shows rainfall spectral signature in terms of scatter plots of  $T_B$ 's at different frequencies. About one year of radiometric observations at ARM SGP site are involved in this plot.  $T_B$ 's from the simulated dataset are shown in black, while measurements are shown in gray (number of points are 35000 for the simulations and 37569 for the measurements). In the top panel, which shows low frequency  $T_B$ 's, non-raining cases are concentrated below 100 K, while raining cases cover the range up to 300 K mainly dominated by hydrometeor emission (see (1)). On the other hand, for higher frequency, non-raining cases are clustered in the middle of the distribution, thus indicating the presence of both emission (i.e.,  $T_B$ 's increase) and scattering (i.e.,  $T_B$ 's decrease) signature mechanisms.

Fig. 5 demonstrates that simulations are able to represent a reasonable range of measured  $T_B$ 's, both for weak absorption (20-30 GHz) and strong absorption (55-60 GHz) frequencies. By comparing simulated and measured data, we can appreciate a similar  $T_B$  behavior. The similarity between the synthetic and the observed data distributions gives us some confidence in using the first as a training set for estimating rain rate from the set of observations.

## IV. RADIOMETRIC ESTIMATION OF RAINFALL

The inversion technique introduced in this work has been developed mainly by focusing on the multispectral nature of MWRP radiometric measurements and on its operational real-time features. Based on previous work [5], [8], [18], we here have developed a new inversion technique suited for the MWRP multispectral observations. Such technique, when trained with simulations and applied to observations, provides estimates of a variety of rainfall parameters, such as columnar hydrometeor content and rain rate. In this work, we do not attempt to estimate a rain water profile, even though in principle it could be performed with some approximations [10]. This potential and capability to easily generalize and extend the results is one of the major advantages of a physically based inversion algorithm with respect to an empirical one.

Radiometer-based rain rate can be validated when measurements from a collocated rain gauge are provided, as discussed in sub-section B. This intercomparison is affected by several problems. Indeed, the type of measurements are profoundly different: one can provide the rain water along a slant column, while the other the accumulated water at a ground point. A major problem concerning rainfall ground-based observation by radiometers is related to the instrument antenna exposure to hydrometeor fall, which can contaminate  $T_B$  measurements. Water films forming on the antenna have resulted with a possible significant impact on observed  $T_B$ 's [11]. The effects on the retrievals of water films on the antenna and an experimental demonstration of how to substantially reduce them by hardware solutions are discussed elsewhere [12], [19]. Here we do not consider such hardware-corrected MWRP data and concentrate on the exploitation of a

statistical estimator sufficiently robust to unknown noise, such as  $T_B$ 's due to antenna water films, being aware that this would imply a slightly less expected accuracy [8].

#### A. INVERSION TECHNIQUE

The inversion procedure, designed for MWRP, is structured in three subsequent steps, specifically extended and tuned for this application but easily extendible to any other sensor configuration. The three foreseen steps are the following:

- i) classify the meteorological background scenario;
- ii) detect rainfall and classify the cloud genera and, eventually, rain regime (stratiform or convective);
- iii) estimate the rain columnar water contents and surface rain rate.

The entire inversion algorithm is formulated in terms of PC's. As justified in the previous section, the first 3 PC's (and EOF's) are sufficient in our case to explain more than 99% of the total variance. The PC transformation has several advantages, mainly its robustness to unknown noise and higher accuracy in best fitting predictands to predictors – the latter feature generally due to the lower degree of non-linearity of the fitting model [21], [9], [20]. These properties have been numerically proven by using the illustrated synthetic dataset as well.

Once a measured  $\mathbf{T}_{Bm}$  vector (where “m” stands for measurement) is available, the measured PC's vector  $\mathbf{P}_{Bm}$  is basically computed by inverting (4), that is:

$$\mathbf{P}_{Bm}^{(c)} = \mathbf{E}^{(c)}(\mathbf{T}_{Bm}^{(c)} - \langle \mathbf{T}_{Bm}^{(c)} \rangle) \quad (3)$$

where  $\mathbf{E}^{(c)}$  is the 3x12 matrix whose rows are represented by the first 3 EOF's and “(c)” stands for the class. Note that, for each classification step, the matrix  $\mathbf{E}$  is different as it is derived from different datasets – for step i), we use 35000 (i.e. 35x1000) records, while for step ii) and iii) we operate on 5000 (i.e. 5x1000) and 1000 records, respectively.

For the first two classification steps, a Maximum *a posteriori* probability (MAP) criterion has been used [8]. Briefly speaking, if  $c$  is the cloud class, then the conditional probability density function (PDF) of considered class  $c$  given a measurement  $\mathbf{P}_{Bm}^{(c)}$  can be expressed through the Bayesian theorem. If the metrics is assumed to be a multivariate Gaussian PDF, then the MAP estimation of cloud class  $c$  reduces to the following maximization:

$$\hat{c} = \text{Mode}_c[-(\mathbf{P}_{Bm}^{(c)} - \mathbf{m}_p^{(c)})^T \mathbf{S}_p^{(c)-1} (\mathbf{P}_{Bm}^{(c)} - \mathbf{m}_p^{(c)}) - \ln(\det \mathbf{S}_p^{(c)}) + 2 \ln p(c)], \quad (4)$$

where  $\mathbf{S}_p^{(c)}$  is the PC-converted measurement auto-covariance matrix of class  $c$  and  $\det$  is the matrix determinant, while  $\mathbf{m}_p^{(c)}$  is the PC mean value vector of class  $c$  and  $p(c)$  represents the *a priori* discrete PDF of class  $c$ . The computation of the mode in (4) requires to know the mean value of the radiometric principal component  $\mathbf{m}_p^{(c)}$  and its auto-covariance  $\mathbf{S}_p^{(c)}$  at each classification step. This statistical characterization of each cloud class can be derived from the generated synthetic data set, while the prior PDF  $p(c)$  can be used to subjectively weight each class as a function of other available information. For simplicity, we have assumed  $p(c)$  as uniform in this work. Note that  $T_B$  (and then PC) probability density is a truncated-Gaussian within each cloud class, but the ensemble of all classes is not necessarily Gaussian [8]. Since we have assumed a Gaussian metrics for each class distance, the inherent error is not critical. The verification of the long-term statistics of each cloud class through measured data is beyond the scopes of this paper and, indeed, not an easy task due to the lack of reference data apart from visual inspections.

As an example of the expected accuracy of the classification step, we have performed a simulated analysis on synthetic measurements, divided in the already mentioned 5 classes (*Cl*, *St*, *Cu*, *Ns*, *Cb*). A similar analysis was also performed in Marzano et al. [8] using window channels only. **Table I** shows the so-called confusion matrix of cloud classification from radiometric data, expressed in error percentage and giving the number of correctly classified clouds on the diagonal and mis-classified clouds on the off-diagonal elements. Elements on the rows are the “true” inputs and those on the columns are the “estimated” outputs. Ideally the confusion matrix should be a diagonal matrix with all elements equal to 100%. The sum of each row is equal to 100%, as expressed by the last column. From Table I it emerges that clear cases are always well detected, while non raining clouds (*St* and *Cu*) are very often mis-classified as clear sky due to their thin

opacity. Stratiform rainfall can be confused with cumulus clouds, while convective rain is fairly well identified.

At step *iii*), after discriminating among cloud class and having identified rain regime, a polynomial regression algorithm can be applied, using the data belonging to the selected rainfall class as a training set. This procedure implies that regression coefficients must be computed for each rainfall class. We have chosen, after an optimization analysis among fitting models, a polynomial expression in terms of selected principal components. Within each class  $c$ , assuming a cubic form, surface rainfall rate  $R^{(c)}$  can be directly estimated from  $T_B$  measurements, converted in PC's through (3), by means of:

$$\hat{R}^{(c)} = a_0 + \sum_{k=1}^3 [a_{1k}^{(c)} P_{Bmk}^{(c)} + a_{2k}^{(c)} (P_{Bmk}^{(c)})^2 + a_{3k}^{(c)} (P_{Bmk}^{(c)})^3], \quad (5)$$

where  $a_{jk}$  ( $j=1:3$ ) are the regression coefficients and  $P_{Bmk}$  stands for the measured  $k$ -th principal component. Similar expressions can be written for columnar hydrometeor contents  $C_h^{(c)}$  (with  $h=c, r, g, i$  for cloud, rain, graupel, and ice hydrometeor, respectively), that is:

$$\hat{C}_h^{(c)} = b_0 + \sum_{k=1}^3 [b_{1kh}^{(c)} P_{Bmk}^{(c)} + b_{2kh}^{(c)} (P_{Bmk}^{(c)})^2 + b_{3kh}^{(c)} (P_{Bmk}^{(c)})^3], \quad (6)$$

being  $b_{jkh}$  ( $j=1:3$ ) the proper regression coefficients.

## B. COMPARISON WITH RAIN GAUGES

A way to check the consistency between modeled and measured data sets is to show the relationship between rain rate and  $T_B$  in the weak absorption region (20-50 GHz), as in **Fig. 6**. Here black dots represent  $T_B$  and rain rate extracted from the overall simulated database, while gray dots correspond to  $T_B$  measured by the MWRP and rain rate estimates obtained from radiometric measurements applying the inversion technique previously described.

In order to assess the quality of our retrieval, we can consider the detection from the MWRP rain binary sensor as a test for the technique to correctly distinguish between rain and no-rain cases. Finally, the quantitative estimate of rain rate can be tested by comparing with measurements from a collocated rain gauge. In **Fig. 7** (left), a time series of about 12 hours of rain rate estimates from MWRP observations is plotted, together with the rain sensor detection. The latter can only be 0 (no rain detected) or 1 (rain detected), although we multiply values by 10 for enhancing the figure clarity. It is evident that the estimate based on radiometric observations senses rain for a shorter period than does the rain detector. Although this might seem to be a rain rate estimator problem, it is actually an advantage of the MWRP technique. In fact, this effect is probably due to residual water droplets laying on top of the MWRP, which are misinterpreted by the rain detector. On the other hand, the retrieval algorithm we have developed is able to interpret this water as residual and to estimate actual rainfall.

**Fig. 7** (right) can further justify this latter explanation since it shows, for the same case study, measurements from the collocated rain gauge. Rain sensor detections are now shown with their original values (0/1), while rain rate estimates had to be averaged into 30-min accumulated rain in order to match the rain gauge time sampling. Rain gauge measurements clearly confirm the duration of the rain shower sensed by radiometric observations, but also show a good quantitative agreement with the radiometric estimates.

Similar to **Fig. 7**, four time series of rain rate at ARM SGP central facility, extending for one to three days, are plotted in **Fig. 8**. Note that averaging for 30 minutes has substantially reduced the dynamical range available for rain rate. By comparing with rain gauge measurements, it is evident that radiometric estimates follow quite well both the detection of rain and the values of rain rates, although there are some differences mainly attributable, in our opinion, to their diverse mode of precipitation sensing.

In order to have a statistical comparison between radiometric estimates and rain gauge measurements we have aligned the two data sets and averaged them into 30-min bins. This filtering operation results in 14,716 bins when both measurements were available. A first analysis concerning the capability of the proposed technique to detect rain is performed on the whole set, and reported in **Table II**. Here we use the statistics indexes as defined in [9] to measure the Probability of Detection of Rain (PODR), the Probability of Detection of No-Rain (PODNR) and the False Alarm Ratio (FAR). From **Table I** we see that the discussed technique shows an excellent PODNR and fairly good PODR and FAR. The last two indexes might be also

slightly affected by time-space variation of the rain field, since the MWRP and the rain gauge were sitting some hundreds meters apart (see Sect. II).

A further analysis concerns the ability of the proposed technique to retrieve quantitatively the value of rain rate, once raining conditions have been detected. Thus, we have limited the set of observations to those classified as rain, a selection which drastically reduces the number of bins to 98. This data set is plotted in **Fig. 9** and has been used to obtain **Table III**. It is evident that there is a fairly good correlation (about 0.82) between the two measurements, although the statistics is limited by the relative small range of variation. The bias and standard deviation of the error are about 0.9 and 1.8 mm, respectively, which results in a root mean square of about 2.0 mm. This error is attributable to the combination of the uncertainty for rain gauge measurements ( $\pm 0.25$  mm, according to the manufacturer), the uncertainty related to the retrieval technique, which depends on the rain rate [8]-[10], but also in large extent to the different features of the two observing systems.

## V. SUMMARY AND FUTURE DEVELOPMENTS

A large set of ground-based multi-frequency radiometric measurements and simulations for different precipitation regimes has been analyzed. The modeled frequencies have been selected in order to match the set of channels currently available on an operational ground-based radiometric system. Rain events occurred in Boulder, Colorado and at the ARM SGP site have been analyzed in terms of comparisons between measurements and model data. This comparison has in a way validated that the observed radiometric signatures can be attributed to rainfall scattering and absorption.

We have discussed and applied a three-step non-linear inversion technique, based on principal components decomposition to estimate rain rate from radiometric observations. This statistical inversion approach is advantageous mainly because of its robustness to unknown noise and higher accuracy in best fitting predictands to predictor. The proposed technique relies on the generated cloud radiative data base to train the non-linear regression algorithm. This feature makes the technique easy to generalize and to extend to applications with other observing systems. The consistency of simulations with both measurements and retrievals has been proven as well.

Retrieval results have been presented comparing time series of radiometric estimates with rain sensor detections and rain gauge measurements. These results are encouraging, showing the potential of this approach, and indicating that the use of the considered radiometric system together with the proposed inversion technique are not too much affected by water films over the antenna. Statistical indexes for rain detection and estimate show reasonable agreement, although the analysis is limited by the relative small range of variation available.

A final remark can be highlighted in terms of a provocative question: do we need a radiometric estimate of rainfall rate at the ground if you can have a gauge there? Would not gauge measurements be more accurate after all? Indeed, we are interested in the rain water content of the atmosphere more than its rate at surface. For historical and practical reasons we need to validate our estimators with rain gauge data, but the aim is not to replace rain gauges but to add estimated rainfall contents to microwave radiometer products as a new feature. This would open to ground-based radiometry a unique potentiality as an all weather instrument for atmospheric monitoring. We hope that the results here presented can contribute to support the use of ground-based multi-frequency microwave radiometry for rain monitoring.

Future developments of this work will regard both modeling and empirical issues. Indeed, the solution of the forward problem might be improved by considering a more sophisticated melting layer and including depolarization effects, while the quality of observations could be further improved if the formation of water film on the antenna is prevented by instrument hardware upgrades (e.g., [11], [12]). Finally, further work shall be devoted to the analysis of a larger set of rainfall cases in various climatological conditions, possibly spanning a larger range of rainfall variation, and to the comparison with other rain sensors, such as weather radars.

## ACKNOWLEDGMENTS

This work has been partially funded by Ministry of Education and Research (MIUR) and by the RISK-AWARE project of INTERREG-IIB CADSES European Commission. Support by the Italian Space Agency (ASI), and by the GNDICI-CNR project is also acknowledged. The authors are grateful to the Guest Editor and three reviewers for their helpful comments and suggestions.

## REFERENCES

- [1] E. R. Westwater (1993), Ground-based microwave remote sensing of meteorological variables in: Janssen, M. A. (ed) *Atmospheric Remote Sensing by Microwave Radiometry*, Wiley, New York
- [2] L. Li, J. Vivekanandan, C.H. Chan, and L. Tsang, "Microwave radiometric technique to retrieve vapor, liquid and ice. Part I: Development of a neural-network based inversion method", *IEEE Trans. Geosci. Remote Sensing*, vol. 35, pp. 224-236, 1997.
- [3] A. Hornbostel and A. Schroth, "Propagation research on the 20 GHz Earth-Olympus satellite path", *J. Electromagn. Waves Appl.*, vol. 9, pp. 439-461, 1995.
- [4] B.E. Sheppard, "Effect of rain on ground-based microwave radiometric measurements in the 20-90 GHz," *J. Atmos. Oceanic Tech.*, vol. 13, pp. 1139-1151, 1996.
- [5] F.S. Marzano, E. Fionda, P. Ciotti, and A. Martellucci, "Rainfall retrieval from ground-based multichannel microwave radiometers", in *Microwave Radiometry and Remote Sensing of the Environment*, P. Pampaloni Ed., VSP Intern. Sci. Publisher, Utrecht (The Netherlands), pp. 397-405, 1999.
- [6] G.R. Liu, C.C. Liu, and T.H. Kuo, , "Rainfall intensity estimation by ground-based dual-frequency microwave radiometers", *J. Appl. Meteor.*, vol. 40, pp. 1035-1041, 2001.
- [7] H. Czekala, , S. Crewell, C. Simmer, A. Thiele, A. Hornbostel and A. Schroth, "Interpretation of polarization features in ground-based microwave observations as caused by horizontally aligned oblate spheroids", *J. Appl. Meteorology*, vol. 40, pp. 1918-1932, 2001.
- [8] F.S. Marzano, E. Fionda, P. Ciotti and A. Martellucci, "Ground-based multi-frequency microwave radiometry for rainfall remote sensing", *IEEE Trans. Geosci. Rem. Sens.*, vol.40, pp.742-759, 2002.
- [9] F.S. Marzano, M. Palmacci, G. Giuliani, D. Cimini, and J. Turk, "Multivariate Statistical Integration of Satellite Infrared and Microwave Radiometric Measurements for Rainfall Retrieval at the Geostationary Scale", *IEEE Trans. Geosci. Rem. Sens.*, vol. 42, pp. 1018-1032, 2004.
- [10] F.S. Marzano, Fionda, E., and Ciotti, P. (1999), "Simulation of radiometric and attenuation measurements along earth-satellite links in the 10 to 50 GHz band through horizontally-finite convective raincells", *Radio Sci.*, vol. 34, pp. 841-858
- [11] M. D. Jacobson, D. C. Hogg, and J. B. Snider, "Wet reflectors in millimeter-wave radiometry-Experiment and theory", *Trans. Geosci. Remote Sensing*, GE-24, pp. 784-791, 1986.
- [12] R. Ware, D. Cimini, P. Herzegh, F.S. Marzano, J. Vivekanandan, and E.R. Westwater, "Ground-based microwave radiometer measurements during precipitation", Proc. of MicroRad04, Rome (Italy), 24-27 Feb., 2004.
- [13] R. Ware, F. Solheim, R. Carpenter, J. Gueldner, J. Liljegren, T. Nehrkorn, and F. Vandenberghe, "A multi-channel radiometric profiler of temperature, humidity and cloud liquid", *Radio Sci.*, vol.38(4), 8079, 1-13, 2003.
- [14] E. A. Smith, P. Bauer, F. S. Marzano, C. D. Kummerow, D. McKague, A. Mugnai and G. Panegrossi, "Intercomparison of microwave radiative transfer models for precipitating clouds", *Trans. Geosci. Remote Sens.*, vol.40, pp.197-203, 2002.
- [15] G. d'Auria, F. S. Marzano, N. Pierdicca, R. Pinna Nossai, P. Basili, and P. Ciotti, "Remotely sensing cloud properties from microwave radiometric observations by using a modeled cloud data base", *Radio Sci.*, vol.33, pp.369-392, 1998.
- [16] H. Liebe, "An atmospheric millimeter-wave propagation model," *Int. J. Infrared & Millimeter-wave*, vol. 10, pp. 367-378, 1989.
- [17] F.S. Marzano, A. Mugnai, E.A. Smith, X. Xiang, J. Turk, and J. Vivekanandan, "Active and passive remote sensing of precipitating storms during CaPE. Part II: Intercomparison of precipitation retrievals from AMPR radiometer and CP-2 radar", *Meteor. Atmospheric Physics*, vol. 54, pp. 29-51, 1994.
- [18] F.S. Marzano, D. Cimini, R. Ware, E. Fionda and P. Ciotti , "Characterization of rainfall signature due to multispectral microwave radiometric data from ground", Proc. of IGARSS03, II: 890 - 892, Toulouse (France), 21-15 July, 2003.
- [19] D. Cimini, F.S. Marzano, R. Ware, E. Fionda and P. Ciotti, "Modeling and measurements of rainfall by ground-based multispectral microwave radiometry", Proc. of MicroRad04, Rome (Italy), 24-27 Feb., 2004.
- [20] P. Basili, P. Ciotti, G. d'Auria, F.S. Marzano, and N. Pierdicca "Simulation study of a microwave radiometric temperature profiler for the Antarctic atmosphere", Proc. of IGARSS 1994, pp. 2436-2438, Pasadena (CA), 27-31 August 1994.
- [21] W. W. Cooley and P. R. Lohnes, *Multivariate Data Analysis*. New York: John Wiley & Sons, 1971.

**Frank Silvio Marzano** [S'89-M'99-SM'03] received the Laurea degree (*cum laude*) in electrical engineering (1988) and the Ph.D. degree (1993) in applied electromagnetics both from the University "La Sapienza" of Rome, Italy. In 1993 he collaborated with the Institute of Atmospheric Physics, CNR, Rome, Italy. From 1994 till 1996, he was with the Italian Space Agency, Rome, Italy, as a post-doctorate researcher. After being a lecturer at the University of Perugia, Italy, in 1997 he joined the Department of Electrical Engineering and the Center of Excellence CETEMPS, University of L'Aquila, Italy teaching courses on electromagnetic fields, antennas and remote sensing. Since 2000 he has been also teaching antennas at the University "La Sapienza" of Rome, Italy. His current research concerns passive and active remote sensing of the atmosphere from ground-based, airborne, and spaceborne platforms, with a particular focus on precipitation using microwave and infrared data, development of inversion methods, radiative transfer modeling of scattering media and radar meteorology issues. He is also involved on radiopropagation topics in relation to incoherent wave modeling, scintillation prediction and rain fading analysis along satellite microwave links. Dr. Marzano is a Senior member *IEEE* and received the Young Scientist Award of XXIV General Assembly of the International Union of Radio Science (URSI) in 1993. In 1998 he was the recipient of the Alan Berman Publication Award (ARPAD) from the Naval Research Laboratory, Washington, DC. From 2001 is the Italian national delegate for the European COST actions n. 720 on atmospheric profiling by ground-based remote sensing and n. 280 on satellite fade mitigation techniques. Since January 2004 he has been acting as an Associated Editor of *IEEE Geoscience Remote Sensing Letters*.

**Domenico Cimini** received the Laurea degree in Physics (*cum laude*) in 1998 and the Ph.D. degree in 2002 both from the University of L'Aquila, L'Aquila, Italy. Since 1999, he collaborated with the Environmental Technology Laboratory (ETL) of National Oceanic and Atmospheric Administration (NOAA), Boulder, CO, USA. During 2000 and 2004, he participated to two Water Vapor Intensive Operational Periods (WVIOP), held at the Atmospheric Radiation Measurement (ARM) program Southern Great Plain (SGP) and North Slope of Alaska (NSA) sites. Since 2002, he has been working with the Center of Excellence CETEMPS, University of L'Aquila, Italy, on radiometer calibration techniques, microwave radiative transfer models and ground- and satellite-based passive microwave and infrared radiometry. Since August 2004, he has been a Visiting Fellow at the Cooperative Institute for Research in Environmental Sciences (CIRES) of University of Colorado, USA.

**Piero Ciotti** received the Laurea (Doctor's) degree in electronic engineering (*cum laude*) from the University of Rome, Italy, in 1977. He joined the Department of Electronic Engineering of the University "La Sapienza" of Rome in 1977 where he served first as an Assistant professor and, since 1987, as a Associate Professor, teaching a course on remote sensing. During 1984-1985, he conducted research at the NOAA/ERL Wave Propagation Laboratory, Boulder, CO, on a NATO/CNR fellowship. He was a member of the ESA Calibration Team for the ERS-1 Radar Altimeter and a Principal Investigator of the ESA/JRC MAESTRO airborne SAR campaign. He is also Principal Investigator of an ESA/ENVISAT accepted research proposal and member of RA-2/MWR, MERIS and SCIAMACHY Calibration Teams. Since 1991 he has been with the Department of Electrical Engineering of the University of L'Aquila, L'Aquila, Italy, where he has taught courses on signal theory, electromagnetic fields, and electromagnetic wave propagation. His research activity has been concerned with radiometric remote sensing of the atmosphere, microwave line-of-sight propagation, inverse electromagnetic problems, and digital signal processing.

**Randolph Ware** serves as President of Radiometrics Corporation. He founded and directed UNAVCO, GPS/MET and SuomiNet at UCAR. He holds a PhD in Nuclear Physics from the University of Colorado. He has published numerous scientific articles and holds patents on atmospheric remote sensing with microwave radiometry and with GPS.

## TABLE CAPTIONS

**Table I:** Confusion matrix of cloud classification, expressed in percentage for Ci, St, Cu, Ns and Cb cloud genera, giving the number of correctly classified clouds on the diagonal and mis-classified clouds on the off-diagonal elements. Rows are inputs and columns are outputs (the sum of each row is equal to 100%, as expressed by the last column).

**Table II:** Statistics indexes for rain detection, as defined in [9]. The entire data set of 14,716 raining and non raining cases has been used for this analysis during the considered year (June 2001 – June 2002)..

**Table III:** Statistics indexes for rain estimate, as defined in [9]. The data set consists of 98 raining cases during the considered year (June 2001 – June 2002).

## FIGURE CAPTIONS

**Figure 1:** An example of the operational MWRP output. Plots refer to data collected during 19 July 2003, in Boulder, Colorado, USA. A rain shower happened roughly at 0400 UTC. Contour plots show time-height cross sections of atmospheric temperature (top), relative humidity (middle) and liquid water (bottom). Surface temperature, relative humidity, and pressure are shown on the left. Infrared cloud temperature, rain detection, integrated content of vapor and liquid are shown on the bottom.

**Figure 2:** Time series of  $T_B$  observed by the MWRP twelve channels during the same event as in Fig. 1. For each channel, the corresponding frequency (GHz) is shown on top of each subplot. It is evident how rainfall greatly effects the low frequency channels (22.2 to 53.8 GHz), while has a relatively small impact on strongly absorbed frequencies (56.6 to 58.8 GHz).

**Figure 3:** Spectral signature in terms of the histograms of  $T_B$  measured by MWRP at different frequencies. The whole data set, spanning over about one year (June 2001 - June 2002), has been used in this plot. In the top panel, which shows low frequency channel  $T_B$ 's, is evident that raining cases are just a small sub sample of the whole data set.

**Figure 4:** First three relevant spectral empirical orthogonal functions (EOF) from the simulated dataset. EOF1 spans 96% of the total variance, while 2% and 1% for EOF2 and EOF3, respectively.

**Figure 5:** Rainfall spectral signature in terms of scatter plots between  $T_B$  at different frequencies. Simulated data set are shown in black, while about one year of measurements (June 2001 – June 2002) are shown in gray.

**Figure 6:** Scatter plots between  $T_B$  and rain rate for the six MWRP lower frequency channels (22.235 to 51.25 GHz). Black dots represent simulated rain rate and  $T_B$ , while gray dots show radiometric observations and the respective rain rate estimates.

**Figure 7:** Left: Time series of MWRP estimated rain rate. Dashed gray line, representing rain sensor detection (0/1), has been multiplied by 10 for convenience. Right: Time series of 30-minute accumulated rain for the same case. Dashed gray line represents rain sensor detection (0/1). Dash-dotted gray line represents measurements from a rain gauge, while the solid black line represents radiometric estimates.

**Figure 8:** More rain events are shown. As in Fig. 6, dash-dotted gray line represents 30-minute accumulated rain as measured by the rain gauge, while the solid black line represents radiometric estimates. Dashed gray line represents the rain sensor detection (0/1).

**Figure 9:** Scatter plot of 30-min accumulated rain (mm) as measured by the rain gauge (SMOS) and as estimated by the MWRP. The sample size is reduced to 98 cases.

**Table I:** Confusion matrix of cloud classification, expressed in percentage for *Cl*, *St*, *Cu*, *Ns* and *Cb* cloud genera. Rows are inputs and columns are outputs (the sum of each row is equal to 100%, as expressed by the last column).

<i>Cloud class</i>	<i>Cl</i>	<i>St</i>	<i>Cu</i>	<i>Ns</i>	<i>Cb</i>	<i>Total (%)</i>
<i>Cl</i>	89	11	0	0	0	100
<i>St</i>	44	36	20	0	0	100
<i>Cu</i>	29	14	56	1	0	100
<i>Ns</i>	1	2	26	69	2	100
<i>Cb</i>	0	0	8	10	82	100

**Table II:** Statistics indexes for rain detection, as defined in [9]. The entire data set of 14,716 raining and non raining cases has been used for this analysis during the considered year (June 2001 – June 2002).

<i>Analysis Index</i>	<i>Acronym</i>	<i>Worst value</i>	<i>Best Value</i>	<i>Value</i>
Probability Of Detection of No Rain	PODNR	0	1	0.99
Probability Of Detection of Rain	PODR	0	1	0.55
False Alarm Ratio	FAR	1	0	0.43

**Table III:** Statistics indexes for rain estimate, as defined in [9]. The data set consists of 98 raining cases during the considered year (June 2001 – June 2002).

<i>Analysis Index</i>	<i>Acronym</i>	<i>Worst value</i>	<i>Best Value</i>	<i>Value</i>
Error Bias [mm/h]	EB	$\pm\infty$	0	0.92
Error Standard Deviation [mm/h]	STD	$\infty$	0	1.80
Error Root Mean Square [mm/h]	RMS	$\infty$	0	2.03
Correlation coefficient	COR	0	1	0.82

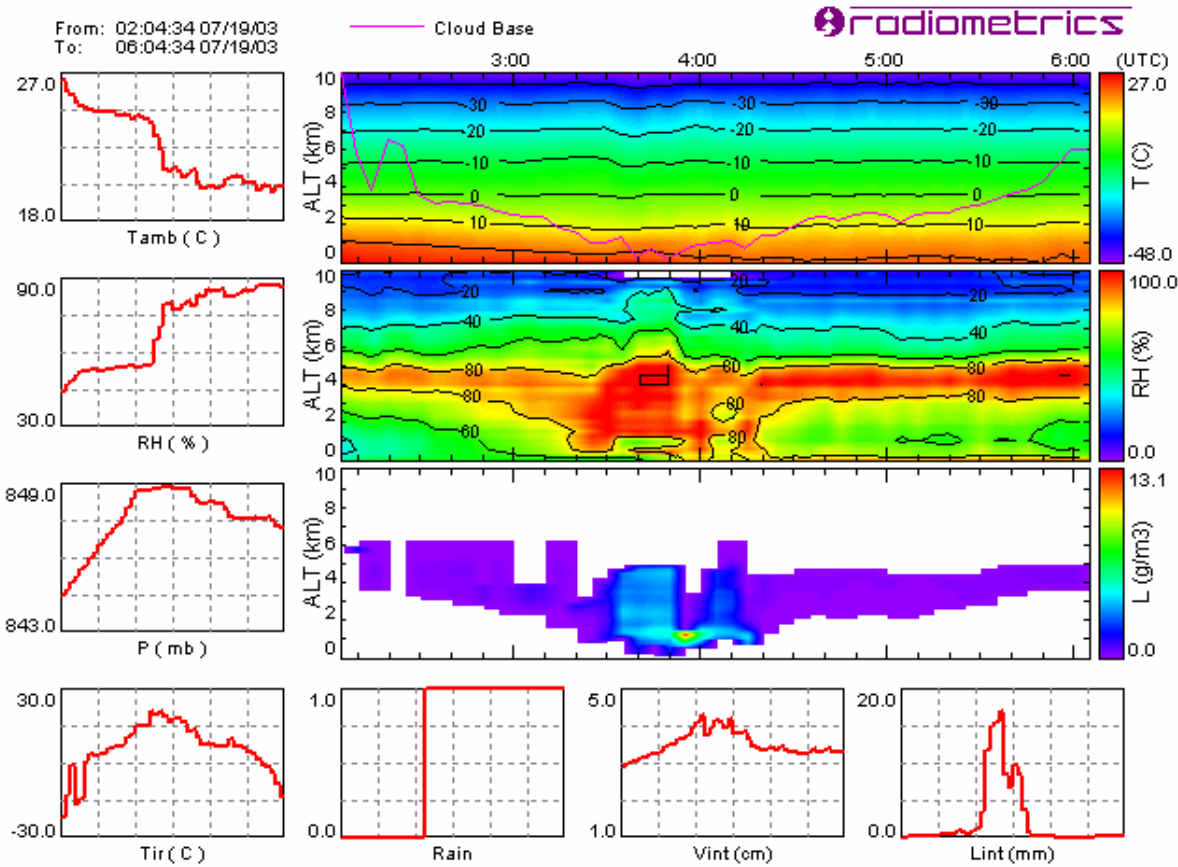


**Figure 1:** An example of the operational MWRP output. Plots refer to data collected during 19 July 2003, in Boulder, Colorado, USA. A rain shower happened roughly at 0400 UTC. Contour plots show time-height cross sections of atmospheric temperature (top), relative humidity (middle) and liquid water (bottom). Surface temperature, relative humidity, and pressure are shown on the left. Infrared cloud temperature, rain detection, integrated content of vapor and liquid are shown on the bottom.

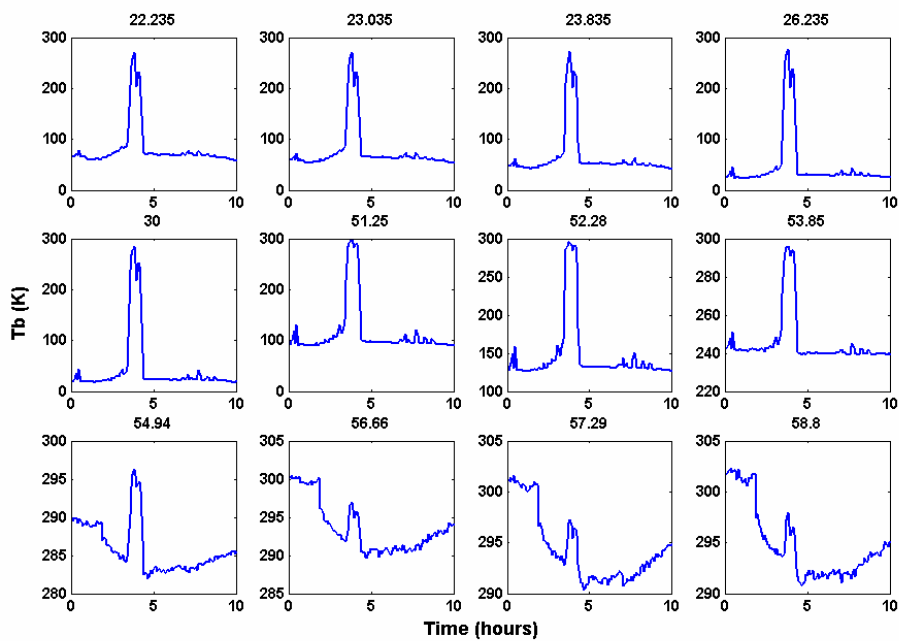


**Figure 2:** Time series of  $T_B$  observed by the MWRP twelve channels during the same event as in Fig. 1. For each channel, the corresponding frequency (GHz) is shown on top of each subplot. It is evident how rainfall

greatly effects the low frequency channels (22.2 to 53.8 GHz), while has a relatively small impact on strongly absorbed frequencies (56.6 to 58.8 GHz).

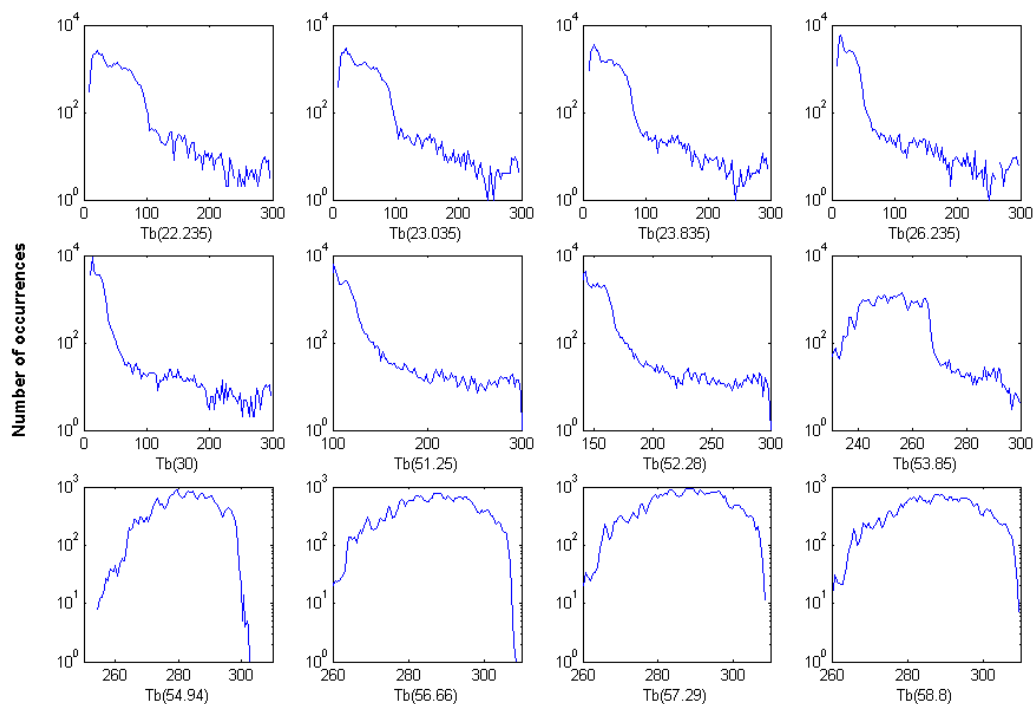


**Figure 3:** Spectral signature in terms of the histograms of  $T_B$  measured by MWRP at different frequencies. The whole data set, spanning over about one year (June 2001 - June 2002), has been used in this plot. In the top panel, which shows low frequency channel  $T_B$ 's, is evident that raining cases are just a small sub sample of the whole data set.

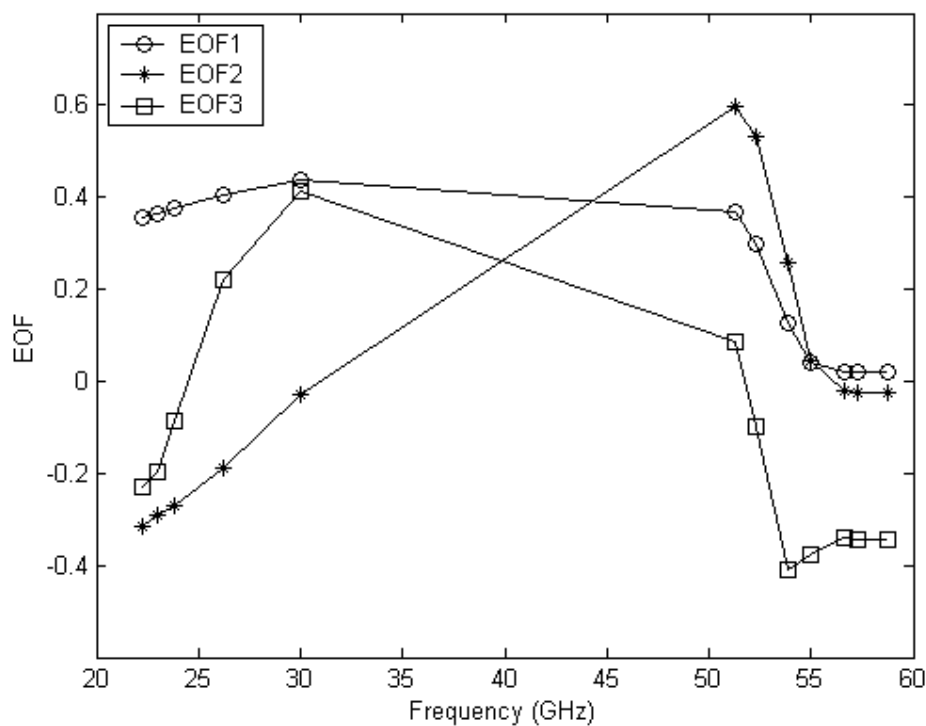


**Figure 4:** First three relevant spectral empirical orthogonal functions (EOF) from the simulated dataset. EOF1 spans 96% of the total variance, while 2% and 1% for EOF2 and EOF3, respectively.

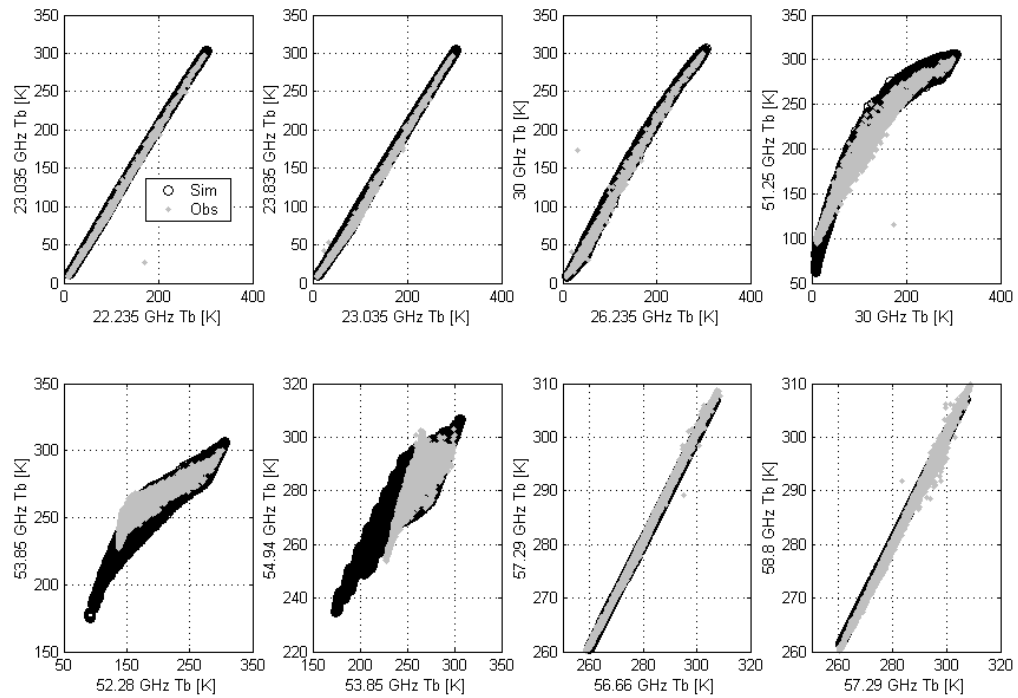


**Figure 5:** Rainfall spectral signature in terms of scatter plots between  $T_B$  at different frequencies. Simulated data set are shown in black, while about one year of measurements (June 2001 – June 2002) are shown in gray.

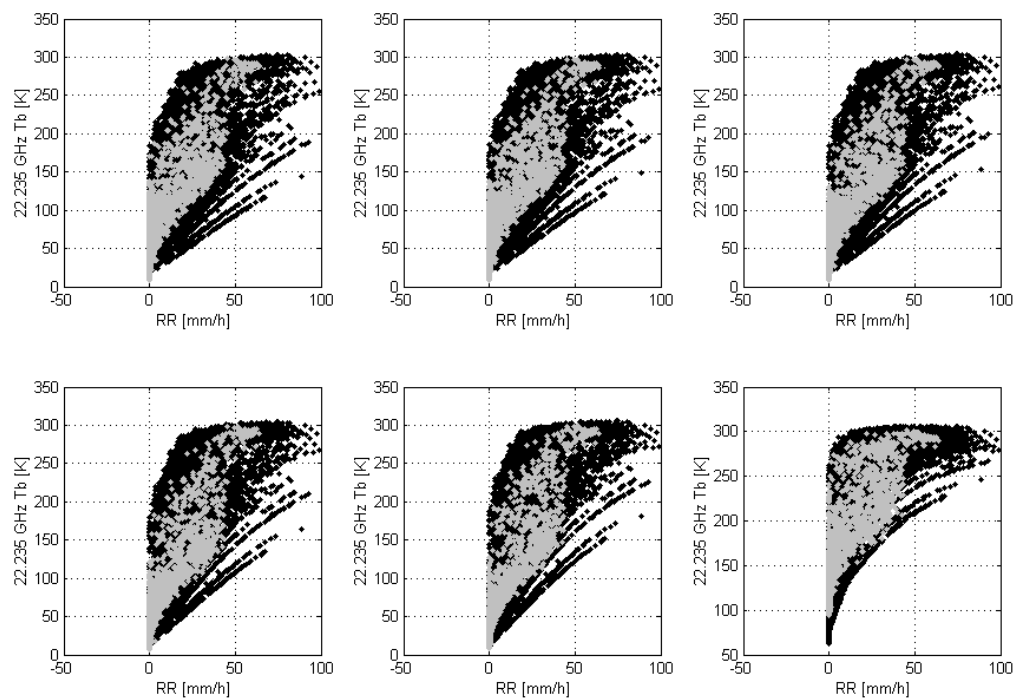


**Figure 6:** Scatter plots between  $T_B$  and rain rate for the six MWRP lower frequency channels (22.235 to 51.25 GHz). Black dots represent simulated rain rate and  $T_B$ , while gray dots show radiometric observations and the respective rain rate estimates.

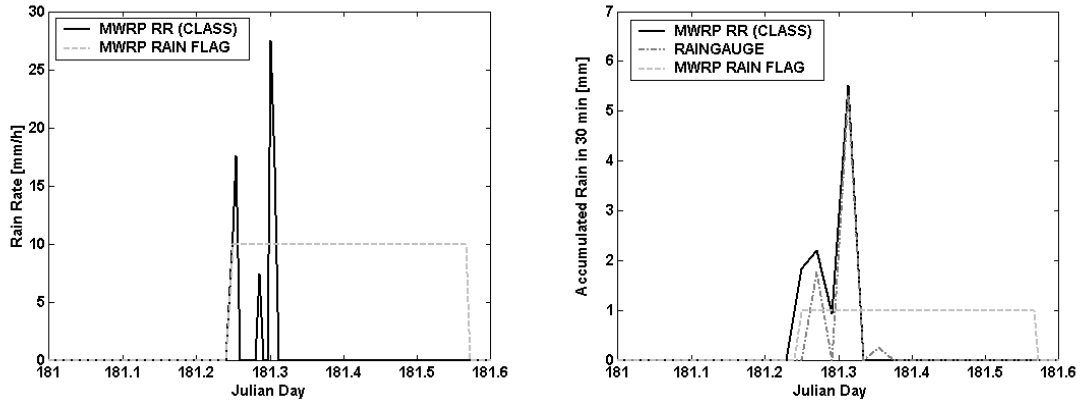


**Figure 7:** Left: Time series of MWRP estimated rain rate. Dashed gray line, representing rain sensor detection (0/1), has been multiplied by 10 for convenience. Right: Time series of 30-minute accumulated rain for the same case. Dashed gray line represents rain sensor detection (0/1). Dash-dotted gray line represents measurements from a rain gauge, while the solid black line represents radiometric estimates.

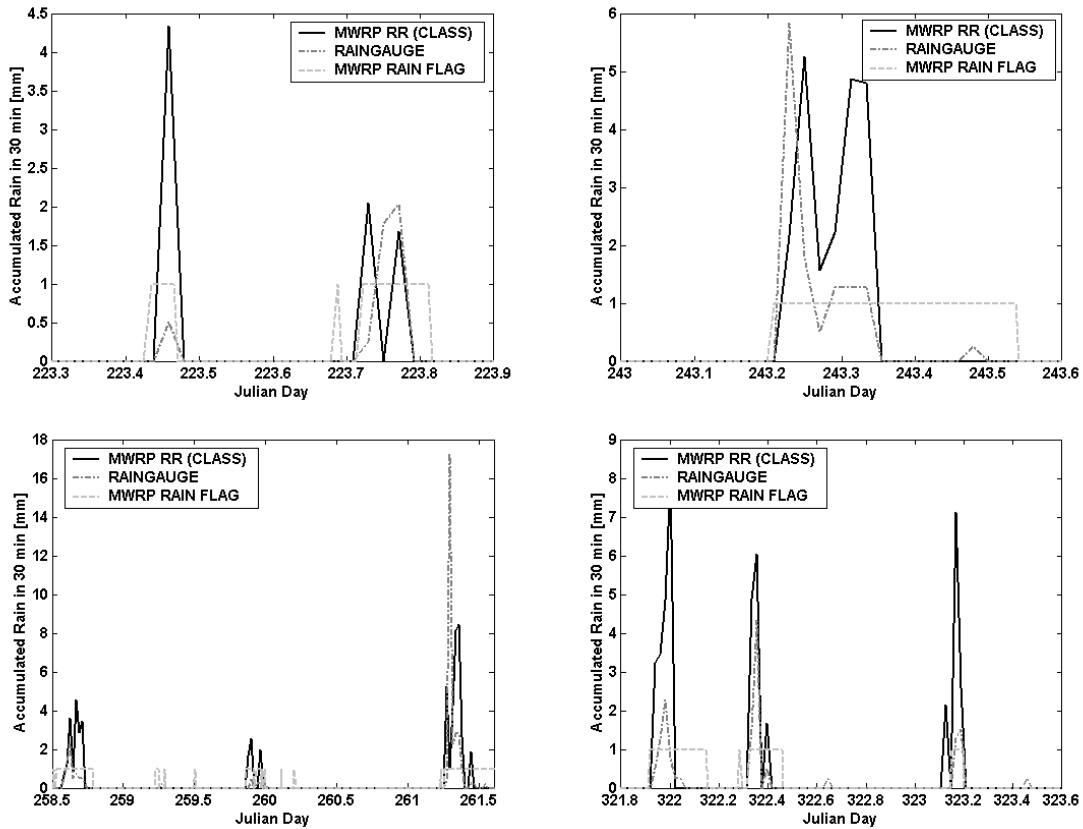


**Figure 8:** More rain events are shown. As in Fig. 6, dash-dotted gray line represents 30-minute accumulated rain as measured by the rain gauge, while the solid black line represents radiometric estimates. Dashed gray line represents the rain sensor detection (0/1).

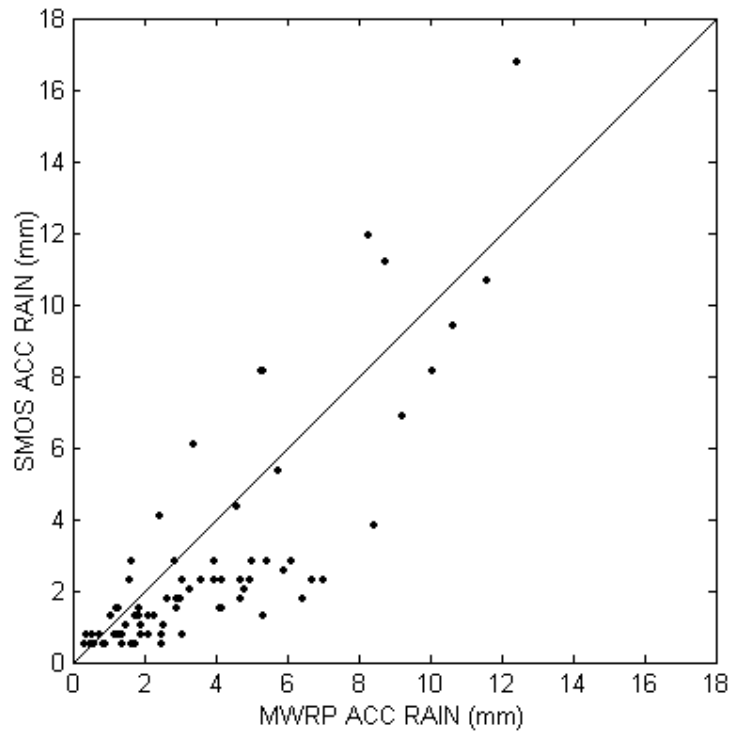


**Figure 9:** Scatter plot of 30-min accumulated rain (mm) as measured by the rain gauge (SMOS) and as estimated by the MWRP. The sample size is reduced to 98 cases.